INTERNATIONAL JOURNAL FOR NUMERICAL METHODS IN FLUIDS
Int. J. Numer. Meth. Fluids 2009; **60**:515–538
Published online 30 September 2008 in Wiley InterScience (www.interscience.wiley.com). DOI: 10.1002/fld.1898

Strongly coupled simulation of fluid–structure interaction in a Francis hydroturbine

W. Q. Wang[1,*,†], X. Q. He[2,‡], L. X. Zhang[1,§], K. M. Liew[2,§] and Y. Guo[3,‡]

[1]*Department of Engineering Mechanics, Kunming University of Science and Technology, Kunming 650051, Yunnan, China*
[2]*Department of Building and Construction, City University of Hong Kong, Tat Chee Avenue, Kowloon, Hong Kong*
[3]*Department of Engineering, University of Aberdeen, Aberdeen AB24 3UE, U.K.*

SUMMARY

This work simulates a complex fluid flow in fluid–structure interaction (FSI). The flow under consideration is governed by Navier–Stokes equations for incompressible viscous fluids and modeled with the finite volume method. Large eddy simulation is used to simulate the unsteady turbulent flow. The structure is represented by a finite element formulation. The present work introduces a strongly coupled partitioned approach that is applied to complex flow in fluid machinery. In this approach, the fluid and structure equations are solved separately using different solvers, but are implicitly coupled into one single module based on sensitivity analysis of the important displacement and stress modes. The applied modes and their responses are used to build up a reduced-order model. The proposed model is used to predict the unsteady flow fields of a 3D complete passage, involving in stay, guide vanes, and runner blades, for a Francis hydro turbine and FSI is considered. The computational results show that a fairly good convergence solution is achieved by using the reduced-order model that is based on only a few displacement and stress modes, which largely reduces the computational cost, compared with traditional approaches. At the same time, a comparison of the numerical results of the model with available experimental data validates the methodology and assesses its accuracy. Copyright © 2008 John Wiley & Sons, Ltd.

Received 1 April 2007; Revised 28 April 2008; Accepted 13 July 2008

KEY WORDS: fluid–structure interaction; strongly coupled approach; reduced-order model; large eddy simulation; hydroturbine passage

*Correspondence to: W. Q. Wang, Department of Engineering Mechanics, Kunming University of Science and Technology, 50 East Ring Road, Kunming 650051, Yunnan, China.
†E-mail: wwqquan@126.com
‡Lecturer.
§Professor.

Contract/grant sponsor: National Natural Science Foundation of China (NSFC); contract/grant number: 50579025

1. INTRODUCTION

The development of electrical engineering and modern hydraulics with increased pressure ratios and reduced weight has led to highly loaded stages with a high speed of inflow. As a result, design engineers often encounter severe hydroelasticity problems, the solution to which can be difficult and costly even with the use of computers. Hence, a valid simulation technique is needed that can be used during the design process to predict correctly the hydroelastic behavior of thin-walled structures in moving water. However, traditional approaches to the analysis of such problems, although extremely useful tools in engineering practice, necessarily rely on simplified models. For example, the fluid flow is often assumed to be a potential flow or a laminar flow, or the deformation of the solid is assumed to be so small that its influence on the fluid flow is negligible; thus, only the fluid stress needs to be applied to the structure and no iteration between the fluid and solid models is required. With the use of these simplified models, the flow features in many kinds of fluid machineries have been intensively studied [1–5] from different aspects by adopting modern fluid numerical technology, such as direct numerical simulation, large eddy simulation (LES), detached eddy simulation, and so forth. However, only few of the flow features in a Francis hydroturbine, an important turbomachinery for electricity generation by water power, have been reported in recent years [6, 7]. Furthermore, studies have concentrated more on the outflow and inflow zones, for example, on the draft tube and the scroll case [8, 9], and the hydroelastic behaviors of runner blades in conjunction with complete passage in a Francis hydroturbine are less researched and reported.

It is well known that the complete passage of a Francis hydroturbine is a highly spatially skewed passage that consists of stay, guide vanes, and runner blades clamped between a crown and a band. A coming flow at high velocity, with strongly distorted wakes due to flow passing the ball valve, the stay vanes and the guide vanes in succession, passes through the runner blade passage at the entrance with an angle of attack. The high curvature of the walls forces the flow to change direction and causes a complicated nonuniform and unsteady turbulent flow, which often induces intensive oscillation of the blade. Inversely, the vibration of the blade has a strong influence on the time–space distributions of the flows near the wall regions. Hence, the time–space evolution character of the turbulent flow in a runner blade passage of a Francis hydroturbine, or the dynamic properties of the runner blade in which the fluid–structure interaction (FSI) is considered, is an important subject in future engineering design.

The main approaches that are employed in the solution of these coupled problems are roughly divided into the monolithic methods [10–13] and the partitioned methods [14–17]. In the monolithic methods, the fluid and the structural equations are strongly coupled and solved together. However, the formulation of a single equation system for the FSI may lead to an increase in the number of degrees of freedom of equations to be solved and the required computations can rapidly increase. Thus, it is fairly difficult to solve these complex engineering problems given the current computational ability of computers. Presently, the monolithic methods are mainly used to solve some simple structures, such as beam, plate and shell structures [18–20].

In the partitioned methods, each field is solved separately and the solution variables are passed iteratively in turn until convergence is achieved. This gives us the flexibility to choose different solvers for each of the modules, but the coupling procedure leads to a loss in accuracy as the modules are updated only after partial or complete convergence. For example, the vibrating blades in a hydroturbine passage are not only separated as moving boundaries of the flow by a loosely dynamical coupling way of iterations in turn between vibration and flow, but more

DOI: 10.1002/fld

computational resource is also wasted and the results are not in good agreement with the measured values [21].

In the present paper, to overcome the above-mentioned drawbacks with the current available soft and hardware resources, we have developed a strongly coupled partitioned method. This is one of the most widely used methods in the field of FSI as it not only paves the way for the use of different solvers for the fluid and structure models, but also couples the solvers in a strong fashion, making this method an efficient one for complex nonlinear problems. For example, for FSI problems that are cast as an abstract differential algebraic equation, some algorithms for strong coupling procedures were developed by Matthies *et al.* [22], Liu *et al.* [23, 24] presented an integrated CFD-CSD code for flutter calculations that is based on a parallel, multiblock, and multigrid flow solver for solving full Navier–Stokes equations. The flow solver is strongly coupled with the structural model dynamics equations, and a dual time-stepping scheme is introduced to enable simultaneous integration of flow and structural equations without a time delay. Nevertheless, the strong coupling method in these papers, which requires costly subiterations at every time-step, can improve the temporal accuracy, but only, of course, if the subiterations converge. Our present work is the development of a new strong coupling of the partitioned approach that is based on sensitivity analysis of the important displacement and stress modes, which is used to construct a reduced-order model that is based on the model of Vierendeels [25]. In this method, the fluid and the structure equations are solved separately using different solvers but are implicitly coupled into one single module. Based on this approach, the hydroelastic behavior of a runner blade in a Francis turbine passage at a high Reynolds number is simulated. The results show that the methodology of the strongly coupled partitioned method is quite effective in overcoming the above-mentioned drawbacks of traditional approaches in hydroelasticity simulations. At the same time, it can achieve a good convergence solution using a reduced-order model that is based on only a few displacement and stress modes, which not only saves computing time but also can enlarge the range of applications in engineering.

2. FUNDAMENTAL EQUATIONS

We consider the flow of an incompressible Newtonian fluid that interacts with an elastic solid. Let Ω_t^{f} be the domain that is occupied by the fluid and Ω_t^{s} be the solid at the time t. Let $\Gamma_t^0 = \Omega_t^{\mathrm{f}} \cap \Omega_t^{\mathrm{s}}$ be the part of the boundary at which the elastic solid interacts with the fluid.

2.1. Fluid properties

A Newtonian incompressible fluid is considered and its state is described by the velocity and the pressure fields u^{f}, p^{f}. The balance equations are

$$\rho^{\mathrm{f}} \frac{\partial u^{\mathrm{f}}}{\partial t} + \rho^{\mathrm{f}} u^{\mathrm{f}} \cdot \nabla u^{\mathrm{f}} = \nabla \cdot \sigma^{\mathrm{f}} \quad \text{in } \Omega_t^{\mathrm{f}} \tag{1}$$

$$\nabla \cdot u^{\mathrm{f}} = 0 \quad \text{in } \Omega_t^{\mathrm{f}} \tag{2}$$

where ∇ is the gradient operator. The material constitutive equation is

$$\sigma^{\mathrm{f}} = 2\mu^{\mathrm{f}} S^{\mathrm{f}} + (-p^{\mathrm{f}} + \lambda^{\mathrm{f}} \nabla \cdot u^{\mathrm{f}}) I \tag{3}$$

DOI: 10.1002/fld

The constant density of the fluid is ρ^{f}, the viscosity is denoted by μ^{f}, I is the unit tensor, and $\lambda^{\mathrm{f}}=-\frac{2}{3}\mu^{\mathrm{f}}$ is constant. The strain-rate tensor of fluid S^{f} is expressed as

$$S^{\mathrm{f}}=\tfrac{1}{2}[(\nabla u^{\mathrm{f}})+(\nabla u^{\mathrm{f}})^{\mathrm{T}}] \tag{4}$$

2.2. Structure properties

The structure is assumed to be an elastic body. Writing in the more common Lagrangian description with respect to some fixed reference (initial) state Ω^{s}, we have

$$\rho^{\mathrm{s}}\frac{\partial^2 u^{\mathrm{s}}}{\partial t^2}=\nabla\cdot(J\sigma^{\mathrm{s}}F^{-\mathrm{T}})+\rho^{\mathrm{s}}g \quad \text{in } \Omega^{\mathrm{s}} \tag{5}$$

where u^{s} is the displacement of structure, ρ^{s} is the density of structure. $F=I+\nabla u^{\mathrm{s}}$ is the deformation gradient tensor.

The material is specified by giving the Cauchy stress tensor σ^{s} (the 2nd Piola–Kirchhoff stress tensor is then given by $S^{\mathrm{S}}=JF^{-1}\sigma^{\mathrm{S}}F^{-\mathrm{T}}$) by the following constitutive law for the St.Venant–Kirchhoff material ($H=\frac{1}{2}(F^{\mathrm{T}}F-I)$):

$$\sigma^{\mathrm{s}}=\frac{1}{J}F(\lambda^{\mathrm{s}}(\operatorname{tr}H)I+2\mu^{\mathrm{s}}H)F^{\mathrm{T}} \tag{6}$$

$$S^{\mathrm{s}}=\lambda^{\mathrm{s}}(\operatorname{tr}H)I+2\mu^{\mathrm{s}}H \tag{7}$$

where $\operatorname{tr}H$ denotes the trace of the matrix H. The elasticity of the material is characterized by Poisson's ratio ν^{s} and by Young's modulus E^{s}. The alternative characterization is described by the Lame coefficients λ^{s} and μ^{s} (the shear modulus)

$$\nu^{\mathrm{s}}=\frac{\lambda^{\mathrm{s}}}{2(\lambda^{\mathrm{s}}+\mu^{\mathrm{s}})}, \quad E^{\mathrm{s}}=\frac{\mu^{\mathrm{s}}(3\lambda^{\mathrm{s}}+2\mu^{\mathrm{s}})}{(\lambda^{\mathrm{s}}+\mu^{\mathrm{s}})} \tag{8}$$

$$\mu^{\mathrm{s}}=\frac{E^{\mathrm{s}}}{2(1+\nu^{\mathrm{s}})}, \quad \lambda^{\mathrm{s}}=\frac{\nu^{\mathrm{s}}E^{\mathrm{s}}}{(1+\nu^{\mathrm{s}})(1-2\nu^{\mathrm{s}})} \tag{9}$$

2.3. Interface conditions

The full interaction conditions between the fluid and the structure are introduced. The geometrical compatibility conditions

$$u^{\mathrm{f}}=u^{\mathrm{s}} \quad \text{on } \Gamma_{\mathrm{t}}^0 \tag{10}$$

and the equilibrium conditions

$$\sigma^{\mathrm{f}}n=\sigma^{\mathrm{s}}n \quad \text{on } \Gamma_{\mathrm{t}}^0 \tag{11}$$

are given, where n is a unit normal vector to the interface Γ_{t}^0. This implies the no-slip condition for the flow and that the forces on the interface are in balance.

DOI: 10.1002/fld

3. COMPUTATIONAL METHOD

3.1. Fluid solver

After applying a filter operation to the unsteady incompressible Navier–Stokes equations (1) and the continuity equation (2) and expressing them in Cartesian component form, the following equations are obtained:

$$\frac{\partial \overline{v}_j^{\mathrm{f}}}{\partial x_j^{\mathrm{f}}} = 0 \tag{12}$$

$$\frac{\partial \overline{v}_i^{\mathrm{f}}}{\partial t} + \frac{\partial}{\partial x_j}(\overline{v}_i^{\mathrm{f}} \overline{v}_j^{\mathrm{f}}) = -\frac{\partial \overline{p}}{\partial x_i} + \frac{\partial}{\partial x_j}\left[v^{\mathrm{f}} \left(\frac{\partial \overline{v}_i^{\mathrm{f}}}{\partial x_j} + \frac{\partial \overline{v}_j^{\mathrm{f}}}{\partial x_i} \right) \right] - \frac{\partial \tau_{ij}^{\mathrm{f}}}{\partial x_j} \tag{13}$$

where $\overline{v}_i^{\mathrm{f}}$ and $\overline{p}$ are the space-averaged velocity and the pressure, respectively, and $\tau_{ij}^{\mathrm{f}} = \overline{v_i^{\mathrm{f}} v_j^{\mathrm{f}}} - \overline{v_i^{\mathrm{f}}}\,\overline{v_j^{\mathrm{f}}}$ is the subgrid-scale (SGS) stress. The standard Smagorinsky model [26] is expressed as

$$\tau_{ij}^{\mathrm{f}} - \frac{\delta_{ij}}{3}\tau_{kk}^{\mathrm{f}} = -2 v_t^{\mathrm{f}} \overline{S_{ij}^{\mathrm{f}}} \tag{14}$$

$$v_t^{\mathrm{f}} = (C_{\mathrm{s}}\Delta)^2 (2\overline{S_{ij}^{\mathrm{f}} S_{ij}^{\mathrm{f}}})^{1/2} \tag{15}$$

where $\overline{S_{ij}^{\mathrm{f}}}$ is the SGS strain-rate tensor, Δ is the characteristic length scale of the largest SGS eddies, δ_{ij} is Kronecker's delta, and $C_{\mathrm{s}} = 0.13$ is based on the model of Mochid *et al.* [27]. To take the near-wall effect into account, the characteristic length scale Δ is multiplied with the van Driest-type wall damping function f [28, 29]

$$f = 1 - \exp\left(-\frac{y^+}{A^+} \right) \tag{16}$$

$$y^+ = \frac{u_\tau y_{\mathrm{p}}}{v^{\mathrm{f}}}, \quad u_\tau = \sqrt{\frac{\tau_{\mathrm{w}}}{\rho^{\mathrm{f}}}}, \quad A^+ = 25 \tag{17}$$

where y^+ is the wall coordinate, A^+ is the empirical constant, u_τ is the wall friction velocity, τ_{w} is the wall shear stress, and y_{p} is the distance from the wall.

The above mathematical model can act as a black box fluid solver, which can prescribe the movement of the boundary of the fluid domain through a user subroutine and also easily extract the stress data at the FSI boundaries. The response of the above flow solver can also be represented by the function Ψ

$${}^{\mathrm{f}}\sigma_{k+1}^{n+1} = \Psi^{n+1}({}^{\mathrm{s}}U_{k+1}^{n+1}) \tag{18}$$

or be expressed as the function Φ

$$\Phi^{n+1}({}^{\mathrm{f}}\sigma_{k+1}^{n+1}, {}^{\mathrm{s}}U_{k+1}^{n+1}) = 0 \tag{19}$$

where ${}^{\mathrm{s}}U_{k+1}^{n+1}$ denotes the prescribed position of the interface boundary nodes that are obtained from the structural solver in subiteration $k+1$ when computing the solution at time level $n+1$.

DOI: 10.1002/fld

It is assumed that the solution at time level n is known. The superscript $n+1$ on Ψ or Φ denotes other variables in the flow solver that are already known at time level $n+1$. Starting from the time level n, the stress distribution on the interface boundary nodes ${}^{\mathrm{f}}\sigma_{k+1}^{n+1}$ can be computed, which is then passed to the structural solver.

3.2. Solid solver

Upon total Lagrangian formulation and finite element discretization, a nonlinear system of equations is obtained in matrix form

$$M^{\mathrm{s}}\ddot{U}_{n+1}^{\mathrm{s}}+C^{\mathrm{s}}\dot{U}_{n+1}^{\mathrm{s}}+K^{\mathrm{s}}U_{n+1}^{\mathrm{s}}=Q_{n+1}^{\mathrm{s}} \tag{20}$$

Here, M^{s} is the mass matrix of the structure, C^{s} is the damping matrix of the structure, K^{s} is the tangent stiffness matrix of the structure, and Q_{n+1}^{s} is the generalized external force vector (including the hydrodynamic loads) at time level $n+1$. $\ddot{U}_{n+1}^{\mathrm{s}}$, $\dot{U}_{n+1}^{\mathrm{s}}$, and U_{n+1}^{s} are the acceleration vector, velocity vector, and the displacement vector of the structure at time level $n+1$, respectively.

In this work, the Newmark algorithm is implemented, which is based on the following approximations at time level $n+1$:

$$\ddot{U}_{n+1}^{\mathrm{s}}=\frac{1}{\beta\Delta t^2}(U_{n+1}^{\mathrm{s}}-U_n^{\mathrm{s}})-\frac{1}{\beta\Delta t}\dot{U}_n^{\mathrm{s}}-\left(\frac{1}{2\beta}-1\right)\ddot{U}_n^{\mathrm{s}} \tag{21}$$

$$\dot{U}_{n+1}^{\mathrm{s}}=\frac{\gamma}{\beta\Delta t}(U_{n+1}^{\mathrm{s}}-U_n^{\mathrm{s}})-\left(\frac{\gamma}{\beta}-1\right)\dot{U}_n^{\mathrm{s}}-\frac{\Delta t}{2}\left(\frac{\gamma}{\beta}-2\right)\ddot{U}_n^{\mathrm{s}} \tag{22}$$

with the time-step size Δt and the Newmark parameters β and γ. Equations (21) and (22) are inserted into (20), noting that the external force that is imposed on the structure is only the hydrodynamic load, and utilizing Equation (11), the structural equation is denoted by function A

$$A^{n+1}({}^{\mathrm{s}}U_{k+1}^{n+1},{}^{\mathrm{f}}\sigma_k^{n+1})=0 \tag{23}$$

for a given stress input ${}^{\mathrm{f}}\sigma_k^{n+1}$ that comes from the fluid solver in subiteration k when computing the solution at time level $n+1$, and neglecting the notation for the update of the boundary condition that is needed in the fluid solver. The superscript $n+1$ on A denotes other variables in the structure solver that are already known at time level $n+1$. The structural solver can also be denoted by function B

$${}^{\mathrm{s}}U_{k+1}^{n+1}=B^{n+1}({}^{\mathrm{f}}\sigma_k^{n+1}) \tag{24}$$

The superscript $n+1$ on Ψ, Φ, A and B, the superscript s on U, and the superscript f on σ are dropped out from now on for convenience.

3.3. Coupled method for both the fluid and the structure solver

When the fluid solver or/and the structure solver is/are black box code/codes, it is not convenient to construct the Jacobian Ψ_U or/and B_σ, which is/are needed to solve the structural or/and fluid problem in an implicit way.

DOI: 10.1002/fld

An implicit structure and fluid solver can be expressed as, respectively,

$$A(U_{k+1}^{n+1}, \sigma_{k+1}^{n+1}) = 0 \tag{25}$$

$$\Phi(\sigma_{k+1}^{n+1}, U_{k+1}^{n+1}) = 0 \tag{26}$$

However, it is possible to construct a reduced-order model of the fluid and the structure solver, respectively, which can be differentiated easily. Let us denote the reduced-order model of the fluid solver and the structural solver by, respectively,

$$\hat{\sigma}_{k+1}^{n+1} = \hat{\Psi}(U_{k+1}^{n+1}) \tag{27}$$

$$\hat{U}_{k+1}^{n+1} = \hat{B}(\sigma_{k+1}^{n+1}) \tag{28}$$

Then, the equations for the structure and the fluid are expressed as, respectively,

$$A(U_{k+1}^{n+1}, \hat{\sigma}_{k+1}^{n+1}) = 0 \tag{29}$$

$$\Phi(\sigma_{k+1}^{n+1}, \hat{U}_{k+1}^{n+1}) = 0 \tag{30}$$

A Newton iteration method can be set up after inserting Equation (27) into Equation (29), and Equation (28) into Equation (30) as follows:

$$A(U_{k+1,\mathrm{s}}^{n+1}, \sigma_{k+1,\mathrm{s}}^{n+1}) + \left(\frac{\partial A}{\partial U} + \frac{\partial A}{\partial \hat{\sigma}}\frac{\partial \hat{\sigma}}{\partial U}\right)(U_{k+1,\mathrm{s}+1}^{n+1} - U_{k+1,\mathrm{s}}^{n+1}) \approx 0 \tag{31}$$

$$\Phi(\sigma_{k+1,\mathrm{f}}^{n+1}, U_{k+1,\mathrm{f}}^{n+1}) + \left(\frac{\partial \Phi}{\partial \sigma} + \frac{\partial \Phi}{\partial \hat{U}}\frac{\partial \hat{U}}{\partial \sigma}\right)(\sigma_{k+1,\mathrm{f}+1}^{n+1} - \sigma_{k+1,\mathrm{f}}^{n+1}) \approx 0 \tag{32}$$

which are solved for $U_{k+1,\mathrm{s}+1}^{n+1}$ and $\sigma_{k+1,\mathrm{f}+1}^{n+1}$ upon convergence, respectively. Note that this iteration procedure with index s or f involves only the solution of the structure or the fluid problems.

The problem can be solved if we have an expression for the Jacobian $\partial\hat{\sigma}/\partial U$ and $\partial\hat{U}/\partial\sigma$ of the reduced-order model for the fluid and the structural problem, which we will denote by $\hat{\Psi}_U$ and $\hat{B}_\sigma$ in the sequel, respectively. Here, we use a reduced-order model for the fluid solver as an example that is based on the model of Vierendeels [25], which is presented below in more detail.

After k subiteration loops, k sets of boundary positions and corresponding stress distribution are obtained that fulfill the flow equations (26). From the moment that the minimum two sets (U_i, σ_i), $i = 1 \ldots k$, are available, a set of displacement modes $D_m = \{d_m, m = 1 \ldots k-1\}$ is constructed with

$$d_m = U_k - U_m \tag{33}$$

The corresponding stress mode to d_m is denoted by $\Delta\sigma_m = \sigma_k - \sigma_m$. A stress mode matrix $\Delta\mathrm{P}_{k-1}$ is constructed as

$$\Delta\mathrm{P}_{k-1} = [\Delta\sigma_1 \ldots \Delta\sigma_{k-1}] \tag{34}$$

in which, the columns contain the computed stress modes.

DOI: 10.1002/fld

An arbitrary displacement ΔU can be projected onto the set of displacement modes D_m. The displacement ΔU can be expressed as

$$\Delta U = \sum_{m=1}^{k-1} \alpha_m d_m + \Delta U_{\text{corr}} \tag{35}$$

where α_m denotes the coordinates of ΔU in the set D_m. Note that the number of displacement modes $(k-1)$ is much smaller than the dimension of ΔU, which explains the correction. The dynamic hydroelastic model of the runner blade is derived from the simplified combination of a finite element model with a nonlinear fluid solver. Often, only the low-frequency eigenmodes of the runner blade are prone to displacement/deformation of the structural system, which may be reduced to only a few bending and torsion modes [30]. Furthermore, it is detected that low-frequency behavior is responsible for the divergence behavior in the model of Vierendeels [25], and therefore, it can be expected that when implicitness is introduced in the subiteration process for a few low-frequency modes, convergence can be obtained. If the displacement modes are well chosen, ΔU can be approximated by $\Delta \widetilde{U}$

$$\Delta U \approx \Delta \widetilde{U} = \sum_{m=1}^{k-1} \alpha_m d_m \tag{36}$$

This is an over-determined problem for the coordinates α_m, which can be faced with the least-squares approach. With this approach, the coordinates α_m can be computed as

$$\begin{bmatrix} \alpha_1 \\ \alpha_2 \\ \vdots \\ \alpha_{k-1} \end{bmatrix} = \begin{bmatrix} \langle d_1, d_1 \rangle & \langle d_1, d_2 \rangle & \cdots & \langle d_1, d_{k-1} \rangle \\ \langle d_2, d_1 \rangle & \langle d_2, d_2 \rangle & \cdots & \langle d_2, d_{k-1} \rangle \\ \vdots & \vdots & & \vdots \\ \langle d_{k-1}, d_1 \rangle & \langle d_{k-1}, d_2 \rangle & \cdots & \langle d_{k-1}, d_{k-1} \rangle \end{bmatrix}^{-1} \begin{bmatrix} d_1^{\mathrm{T}} \\ d_2^{\mathrm{T}} \\ \vdots \\ d_{k-1}^{\mathrm{T}} \end{bmatrix} \Delta U \tag{37}$$

The coordinates α_m denote the amount of each mode in the displacement ΔU, so the corresponding change in stress $\Delta \sigma$ can be approximated as

$$\Delta \sigma \approx \alpha \Delta \mathrm{P}_{k-1} = \sum_{m=1}^{k-1} \alpha_m \Delta \sigma_m \tag{38}$$

Equation (37) is inserted into Equation (38), and the Jacobian $\hat{\Psi}_U$ of the reduced-order model can thus be expressed as

$$\hat{\Psi}_U = [\Delta\sigma_1, \Delta\sigma_2 \ldots \Delta\sigma_{k-1}] \begin{bmatrix} \langle d_1, d_1 \rangle & \langle d_1, d_2 \rangle & \cdots & \langle d_1, d_{k-1} \rangle \\ \langle d_2, d_1 \rangle & \langle d_2, d_2 \rangle & \cdots & \langle d_2, d_{k-1} \rangle \\ \vdots & \vdots & & \vdots \\ \langle d_{k-1}, d_1 \rangle & \langle d_{k-1}, d_2 \rangle & \cdots & \langle d_{k-1}, d_{k-1} \rangle \end{bmatrix}^{-1} \begin{bmatrix} d_1^{\mathrm{T}} \\ d_2^{\mathrm{T}} \\ \vdots \\ d_{k-1}^{\mathrm{T}} \end{bmatrix} \tag{39}$$

The reduced-order model that is used in subiteration $k+1$ for the fluid solver is expressed as

$$\hat{\sigma}_{k+1}^{n+1} = \sigma_k^{n+1} + \hat{\Psi}_U (U_{k+1}^{n+1} - U_k^{n+1}) \tag{40}$$

So far, the construction of the reduced-order model for the fluid solver is completed.

DOI: 10.1002/fld

In the same way, the Jacobian $\hat{B}_\sigma$ of the reduced-order model for the structure solver can be expressed as

$$\hat{B}_\sigma = [d_1, d_2 \ldots d_{k-1}] \begin{bmatrix} \langle \Delta\sigma_1, \Delta\sigma_1 \rangle & \langle \Delta\sigma_1, \Delta\sigma_2 \rangle & \cdots & \langle \Delta\sigma_1, \Delta\sigma_{k-1} \rangle \\ \langle \Delta\sigma_2, \Delta\sigma_1 \rangle & \langle \Delta\sigma_2, \Delta\sigma_2 \rangle & \cdots & \langle \Delta\sigma_2, \Delta\sigma_{k-1} \rangle \\ \vdots & \vdots & & \vdots \\ \langle \Delta\sigma_{k-1}, \Delta\sigma_1 \rangle & \langle \Delta\sigma_{k-1}, \Delta\sigma_2 \rangle & \cdots & \langle \Delta\sigma_{k-1}, \Delta\sigma_{k-1} \rangle \end{bmatrix}^{-1} \begin{bmatrix} \Delta\sigma_1^{\mathrm{T}} \\ \Delta\sigma_2^{\mathrm{T}} \\ \vdots \\ \Delta\sigma_{k-1}^{\mathrm{T}} \end{bmatrix} \tag{41}$$

The reduced-order model that is used in subiteration $k+1$ for the solid solver is expressed as

$$\hat{U}_{k+1}^{n+1} = U_k^{n+1} + \hat{B}_\sigma(\sigma_{k+1}^{n+1} - \sigma_k^{n+1}) \tag{42}$$

As described above, the reduced-order model for the fluid solver is built up from sets of positions (U_k^{f}) and the corresponding stress distribution (σ_k^{f}). At the same time, the reduced-order model for the solid solver is also built up from sets of stress distribution ($\sigma_{k'}^{\mathrm{s}}$) and the corresponding interface boundary position distribution ($U_{k'}^{\mathrm{s}}$). The superscript $n+1$ is omitted in the next part and the superscripts f and s are introduced to distinguish the fluid and the structure solver.

After k' structure solver calls and k fluid solver calls, the reduced-order models for the structure and the fluid solvers can be expressed as, respectively,

$$\hat{U}_{k'+1}^{\mathrm{s}} = U_{k'}^{\mathrm{s}} + \hat{B}_\sigma(\sigma_{k'+1}^{\mathrm{s}} - \sigma_{k'}^{\mathrm{s}}) \tag{43}$$

$$\hat{\sigma}_{k+1}^{\mathrm{f}} = \sigma_k^{\mathrm{f}} + \hat{\Psi}_U(U_{k+1}^{\mathrm{f}} - U_k^{\mathrm{f}}) \tag{44}$$

where we use the interface conditions of Equations (10) and (11), a solution for $[\hat{U}\ \hat{\sigma}]^{\mathrm{T}}$ is sought that fulfills both equations, i.e. $\hat{U} = \hat{U}_{k'+1}^{\mathrm{s}} = U_{k+1}^{\mathrm{f}}$ and $\hat{\sigma} = \hat{\sigma}_{k+1}^{\mathrm{f}} = \sigma_{k'+1}^{\mathrm{s}}$. The solution can be expressed as

$$\begin{bmatrix} \hat{U} \\ \hat{\sigma} \end{bmatrix} = \left(I - \begin{bmatrix} 0 & \hat{B}_\sigma \\ \hat{\Psi}_U & 0 \end{bmatrix} \right)^{-1} \left(\begin{bmatrix} U_{k'}^{\mathrm{s}} \\ \sigma_k^{\mathrm{f}} \end{bmatrix} - \begin{bmatrix} 0 & \hat{B}_\sigma \\ \hat{\Psi}_U & 0 \end{bmatrix} \begin{bmatrix} U_k^{\mathrm{f}} \\ \sigma_{k'}^{\mathrm{s}} \end{bmatrix} \right) \tag{45}$$

This solution can be obtained each time before the fluid or the structure solver is called and this solution can then be used as input for these calls. However when calling the fluid solver only the solution for $\hat{U}$ is needed, and when the structure solver is called only the solution for $\hat{\sigma}$ has to be obtained. Equations (43) and (44) can be solved for $\hat{U}$:

$$\hat{U} = (I - \hat{B}_\sigma \hat{\Psi}_U)^{-1}[U_{k'}^{\mathrm{s}} + \hat{B}_\sigma(\sigma_k^{\mathrm{f}} - \sigma_{k'}^{\mathrm{s}} - \hat{\Psi}_U U_k^{\mathrm{f}})] \tag{46}$$

or for $\hat{\sigma}$:

$$\hat{\sigma} = (I - \hat{\Psi}_U \hat{B}_\sigma)^{-1}[\sigma_k^{\mathrm{f}} + \hat{\Psi}_U(U_{k'}^{\mathrm{s}} - U_k^{\mathrm{f}} - \hat{B}_\sigma \sigma_{k'}^{\mathrm{s}})] \tag{47}$$

Once the $\hat{U}$ and $\hat{\sigma}$ are gained, the responses to fluid solution $\sigma_{k+1}^{\mathrm{f}}$ and structural solution U_{k+1}^{s} using the fluid solver equation (30) and the solid solver equation (29), respectively, are computed, then the residual

$$r_{k+1} = A(U_{k+1}^{\mathrm{s}}, \sigma_{k+1}^{\mathrm{f}}) \tag{48}$$

is computed until the convergence criterion is satisfied.

DOI: 10.1002/fld

3.4. Solution program

Given the solution at the time instant t_n and the time-step $\Delta t = t_{n+1} - t_n$, on the basis of the solution at t_n, an initial guess is made for ${}^{\mathrm{f}}U_1^{n+1}$ at t_{n+1}, namely,

$$ {}^{\mathrm{f}}U_1^{n+1} = {}^{\mathrm{s}}U^n + {}^{\mathrm{s}}V^n \Delta t \tag{49}$$

Next, the stress of the fluid nodes ${}^{\mathrm{f}}\sigma_1^{n+1}$ is computed with the fluid solver, then assuming ${}^{\mathrm{s}}\sigma_1^{n+1} = {}^{\mathrm{f}}\sigma_1^{n+1}$, the structural displacement ${}^{\mathrm{s}}U_1^{n+1}$ is gained with the structure solver. Then ${}^{\mathrm{f}}U_2^{n+1}$ is gained by underrelaxing the displacement $\Delta U_1^{n+1} = {}^{\mathrm{s}}U_1^{n+1} - {}^{\mathrm{f}}U_1^{n+1}$ with a factor ϕ, namely,

$$ {}^{\mathrm{f}}U_2^{n+1} = {}^{\mathrm{f}}U_1^{n+1} + \phi \Delta U_1^{n+1}, \quad (0 < \phi < 1) \tag{50}$$

computing the corresponding stress distribution ${}^{\mathrm{f}}\sigma_2^{n+1}$, assuming ${}^{\mathrm{s}}\sigma_2^{n+1} = {}^{\mathrm{f}}\sigma_2^{n+1}$, the structural displacement ${}^{\mathrm{s}}U_2^{n+1}$ is gained with the structure solver.

After at least two sets of interface boundary positions and corresponding stress distributions are gained, the kth reduced-order model for the structure and fluid solver can be constructed using the $(k-1)$th modes via Equations (43) and (44), respectively. Next, compute the reduced $(k+1)$th structural displacement and fluid boundary nodes stress using Equations (46) and (47), respectively, then solve the fluid equation (30) and structure equation (29) using the reduced $(k+1)$th structural displacement and fluid boundary nodes stress, respectively, and gain the true $(k+1)$th fluid boundary nodes stress and structural displacement. Finally, compute the residual via Equation (48), checking whether or not the convergence criterion is satisfied. If it is not satisfied, the unknowns are updated, and the complete procedure is repeated for the improved values of U and σ until the convergence criterion is satisfied. A summary of the algorithm is given in Figure 1.

4. NUMERICAL EXAMPLE

The numerical example is a runner blade of a test Type-A55x Francis hydroturbine model. The opening of the guide vanes is 22 mm. The material parameters of the fluid and the runner blade are listed in Table I.

4.1. Computational setup

The computational domain, including the distributor (stay vanes and guide vanes) domain and the runner domain, is shown in Figure 2, and consists of one stay vane, one guide vane, and a runner blade. The distributor computational domain corresponds to an inter-blade channel that is bounded upstream by a cylindrical patch A-A and downstream by a conical patch B-B. The distributor inlet section corresponds to the spiral casing outlet section, whereas the outlet section is conventionally considered to be the distributor–runner interface. The runner computational domain also corresponds to an inter-blade channel that is bounded upstream by a conical patch (wrapped on the same conical surface as the distributor outlet), then across the runner middle axis C-C, and is extended downstream up to the draft tube inlet of radius D-D. For separation of the made-up turbulence that is caused by the strong 3D skewing passage, including the runner blade oscillation, the runner rotation is not required in our first stage of research. The geometry is normalized with

DOI: 10.1002/fld

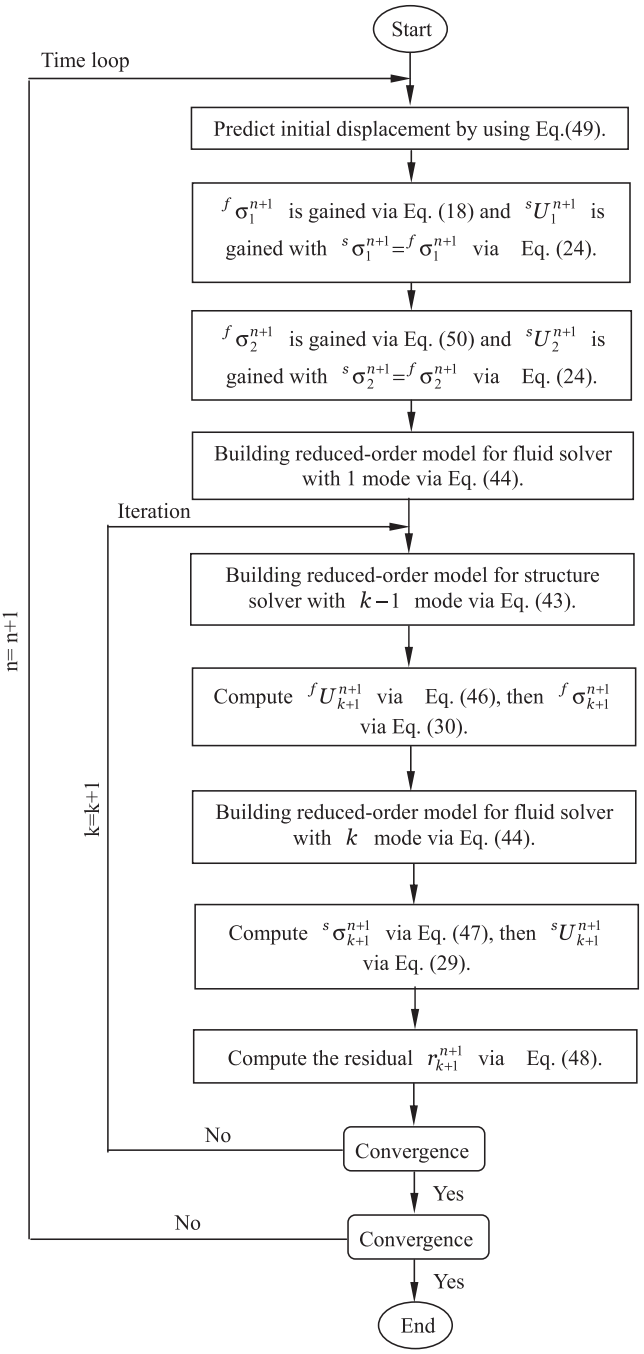

Figure 1. Computational process for the coupled system.

DOI: 10.1002/fld

Table I. Fluid and solid material properties.

Properties	Value
Mass density, ρ^{f}	$1.0\times10^{3}\,\mathrm{kg/m^3}$
Kinematic viscosity, μ^{f}	$1.06\times10^{-3}\,\mathrm{kg/ms}$
Mass density, ρ^{s}	$1.28\times10^{3}\,\mathrm{kg/m^3}$
Young's modulus, E^{s}	$2.5\,\mathrm{GN/m^2}$
Poisson's ratio, v^{s}	0.348

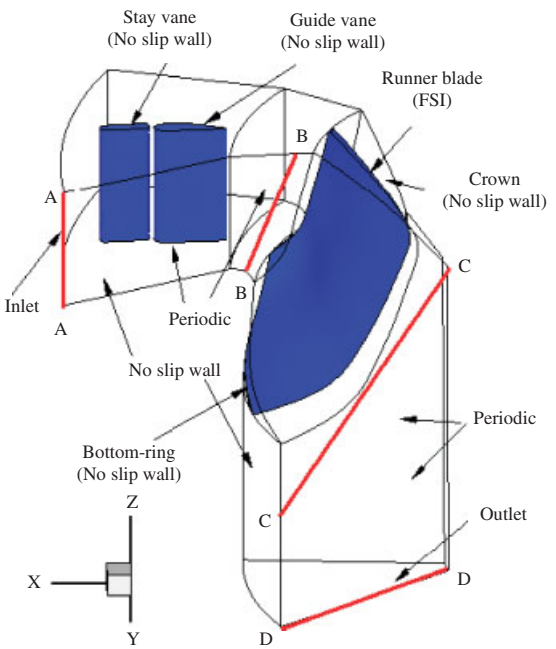

Figure 2. The geometric configuration, computational domain, and boundary conditions.

half of the external diameter of the runner blade, $R_{\mathrm{ref}}=0.225\,\mathrm{m}$. The mean chord dimension L of the runner blade passage (streamwise dimension) is prescribed as $L/R_{\mathrm{ref}}=0.724$ and the mean blade-pitch dimension as $y/R_{\mathrm{ref}}=0.46$ and the mean spanwise dimension of the blade passage is prescribed as $z/R_{\mathrm{ref}}=2.06$. The mean coming flow velocity at the inlet of the runner domain (B-B) passage is defined as reference velocity $U_{\mathrm{ref}}=1.43\,\mathrm{m/s}$. The flow Reynolds number is defined as $Re=U_{\mathrm{ref}}L/v^{\mathrm{f}}=2.2\times10^{5}$.

The meshes around the runner blade surfaces are first generated and then the other domains are calculated in turn. The tetrahedral fluid element number is 1.55×10^{6} and 36 186 nodes are distributed over one side of the blade surfaces (averaging 163 points in the streamwise direction and 222 points in the spanwise direction). For the structure a 3D solid element is used and a

DOI: 10.1002/fld

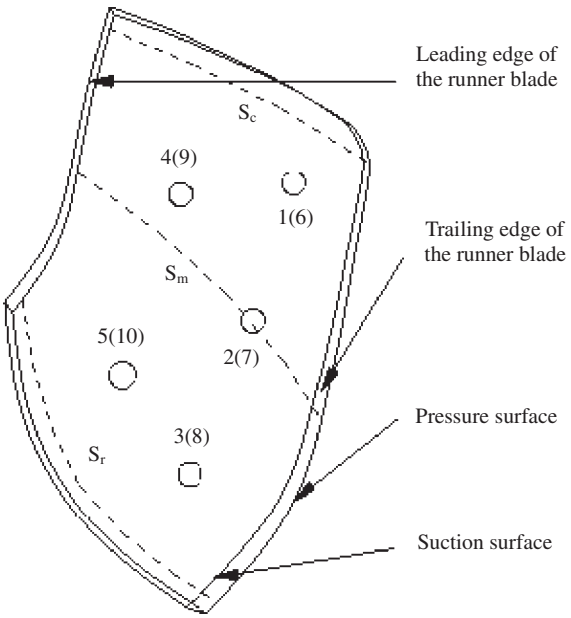

Figure 3. The measured points and distribution of the computational characteristic lines on the runner blade surface.

four-faced tetrahedral element is constructed, and the total number of nodes is 792 (averaging 24 points in the streamwise direction and 33 points in the spanwise direction) over one side of the runner blade surfaces.

The computational boundary conditions are shown in Figure 2 and are presented as follows. A uniform velocity field that is normal at the inflow section is imposed on the distributor inlet section and a random 2D vortex method boundary condition proposed by Sergent *et al.* [31] is used to reconstruct the turbulent fluctuations (the turbulence intensity is 6% and turbulence length scale is $l = 0.07R = 0.003\,\mathrm{m}$, where R is the hydroradius of the distributor inlet section). The free outflow condition is specified on the runner outlet (draft tube inlet), the periodic conditions are imposed on the pitchwise periodic boundary, and no-slip wall conditions are imposed on the stay, guide, and distributor upper and lower rings as well as on the crown and band surfaces of the runner blade, respectively. The FSI conditions are applied to the pressure and suction surfaces of the runner blade, which is shown in Figure 3.

4.2. Numerical convergence behavior

Figure 4(a) shows in detail the number of modes that are used per time-step in a stable vibrating periodic. The maximum number of modes used is six, which largely decreases the coupled iterating numbers.

Figure 4(b) shows the convergence result for two classic time-steps in a stable vibrating periodic (time-step 20; slowest convergence and time-step 185; fast convergence). It is seen that the reduced-order model illustrates good convergence behavior.

DOI: 10.1002/fld

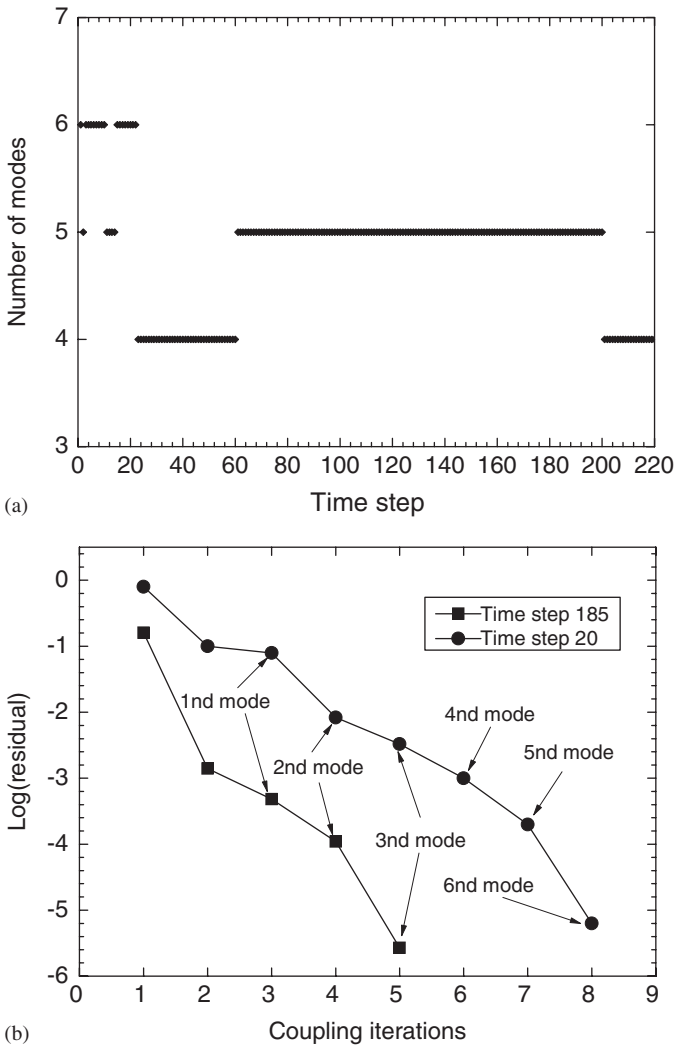

Figure 4. The numerical convergence behavior during a stable computational period T: (a) the number of modes used in each time and (b) the convergence behavior of the subiteration process for two time steps, 20 and 185.

4.3. Numerical results

To present the difference between the case in which the FSI is not considered and that in which it is considered, two computational examples are presented: one with fluid flow over a stationary runner blade and another with fluid flow over a runner blade that is vibrating due to FSI. A changeable time interval is adopted to simulate progress for convergence and accuracy. The maximum time-step is limited to less than $4.5 \times 10^{-3} T$ ($T = L/U_{\text{ref}}$ as the passing period of the blade passage).

DOI: 10.1002/fld

The total simulation time is $13T$ and collection of the sampling data for time statistics starts from $4T$.

The time-averaged vibrating amplitudes along different characterized lines on the runner blade are shown Figure 5. The deformation gradually increases from the leading edge to the trailing edge and it is up to the maximum in the trailing edge. Figure 5(b) shows that the deformation is

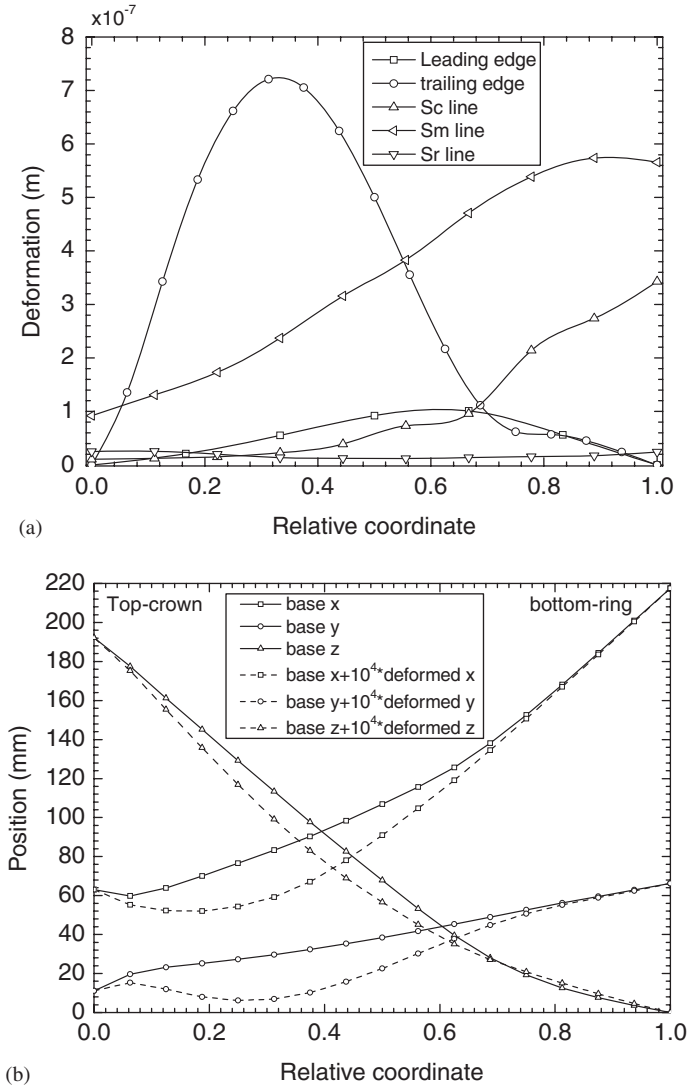

Figure 5. The deformation of the runner blade during a stable computational period T: (a) the deformation magnitude of the blade along different characterized lines and (b) the deformation position along the trailing edge.

DOI: 10.1002/fld

mainly intensive in the pitchwise direction and the spanwise deformation is small relative to the pitchwise and streamwise deformation. Simultaneously, the deformation of the runner blade along the Sm line (near the middle) is far larger than that along the Sc (near the crown) and the Sr (near the band) lines and the deformation is up to the minimum along the Sr line.

The pressure distributions along the suction and pressure sides of the runner blade in the time-averaged static pressure coefficient $C_p = 2(\overline{p} - \overline{p}_{out})/\rho^f U_{ref}^2$ are shown in Figure 6, where $\overline{p}_{out}$ is the time-averaged static pressure in the outlet section (draft tube inlet D-D section) of the computational domain based on the area-weighted average. One can see that the turbulence computations for both the case in which FSI is considered and that in which it is not considered predict nearly the same results, but the maximum and minimum pressures along the three characterized lines are different, especially in the zones near the leading edge of the runner blade. This is an interesting result, as it shows that even a small change of the flow angle on the runner inflow can greatly influence the flow fields. It also shows that the computation in which FSI is considered is more reliable.

The time-averaged skin friction coefficient distributions along the suction and pressure sides of the runner blade in three different characterized lines, $C_f = 2\tau_w/\rho^f U_{ref}^2$, are shown in Figure 7. The skin friction coefficient distributions along the Sc line and the Sm line on the pressure and suction surfaces in the two cases show the same trend, but the skin friction coefficient along the Sr line on the pressure surface is quite different near the bottom ring of the runner blade, which is due to the large deformation of the runner blade, and affects the eddy that is shed along the outlet of the runner blade passage.

Figure 8 shows the static pressure distribution that is based on the time-averaged root-mean-square (RMS) on the pressure and suction surfaces of the runner blade. The pressure contour lines are basically equidistant, and the pressure distributions are divided into three zones. The first is a short adverse pressure gradient region near the leading edge of the blade passage, the second is an acceleration zone from the crown to the trailing edge, and the third is an acceleration zone from the leading to the trailing edge along the bottom ring. Some differences in local zones are also seen between the case in which FSI is considered and in which it is not. For example, when FSI is considered, at the inflow domain near the pressure side, a high-pressure and a low-pressure band are formed along the spanwise direction, which is led by intense spanwise vortex pairs, whereas there is mainly a low-pressure region in the inflow zones when FSI is not considered.

Figure 9 shows the velocity magnitude distribution that is based on the RMS near the pressure and suction sides. Some self-closed contour lines are exhibited on these sections, which is why there is a strong swirling flow at these zones. High velocity and large velocity gradients appear in the trailing zones. In the other zones, the contour lines are equidistant. The contour of the velocity magnitude is very uneven in the near bottom-ring zones on the suction side, which shows that the flow in the bottom-ring zones near the suction side is very unstable. The large difference of the velocity distributions that is based on the RSM between the case in which FSI is considered and that in which it is not is clearly shown, which inefficiently tests the sensitivity of the flow velocity distribution to the deformation of the runner blade.

4.4. Comparison of numerical and experimental results

To validate our methodology and to assess the accuracy of the numerical results, we have performed extensive comparisons with available experimental results. The pressure sensors that are made by UAS Kulite, LL-072-25A, were mounted on the pressure and suction sides of the blade as shown

DOI: 10.1002/fld

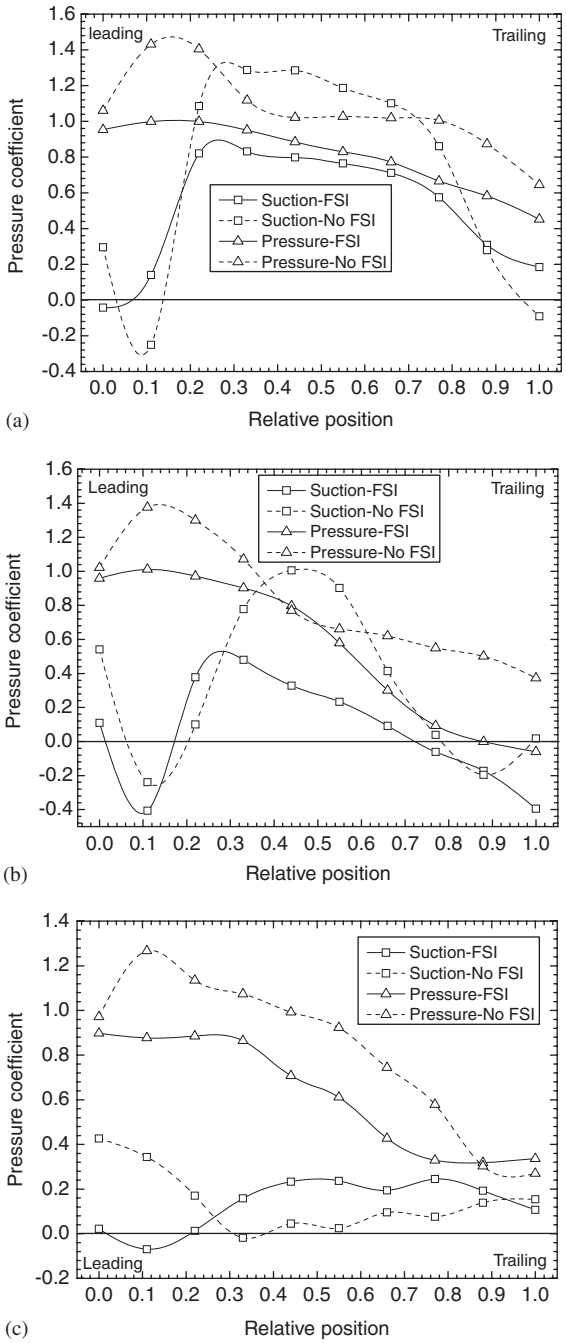

Figure 6. Time-averaged pressure distribution along different characterized lines: (a) along Sc line; (b) along Sm line; and (c) along Sr line.

DOI: 10.1002/fld

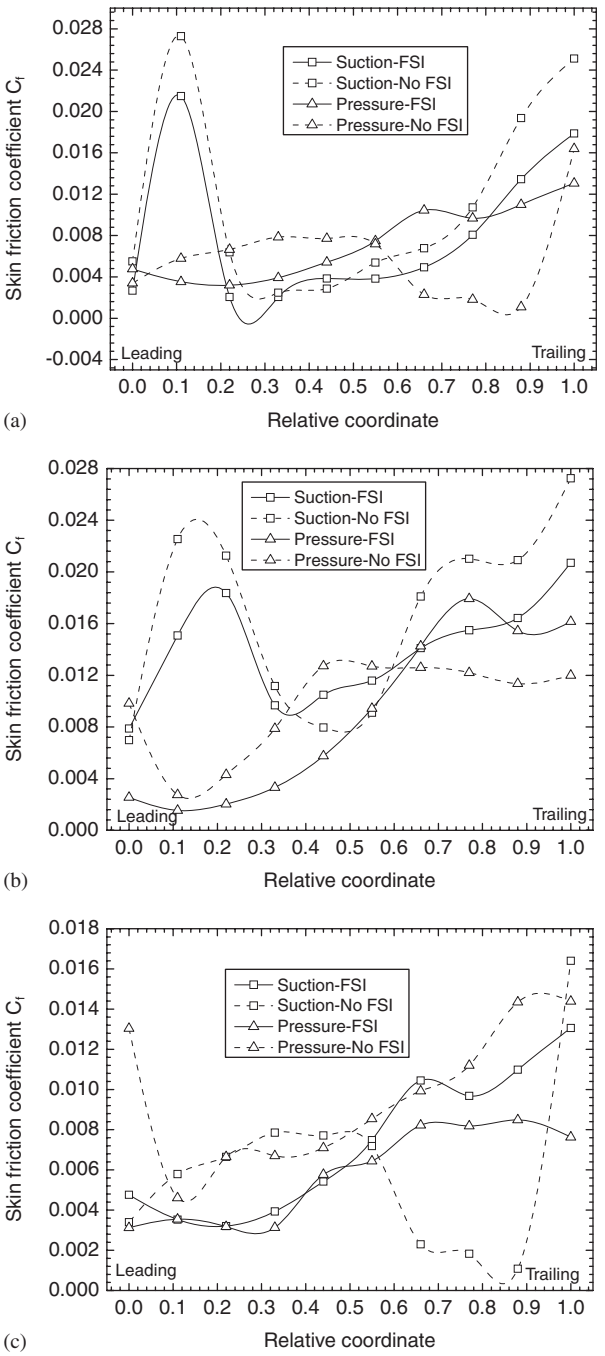

Figure 7. Time-averaged skin friction coefficient distribution along different characterized lines: (a) along Sc line; (b) along Sm line; and (c) along Sr line.

DOI: 10.1002/fld

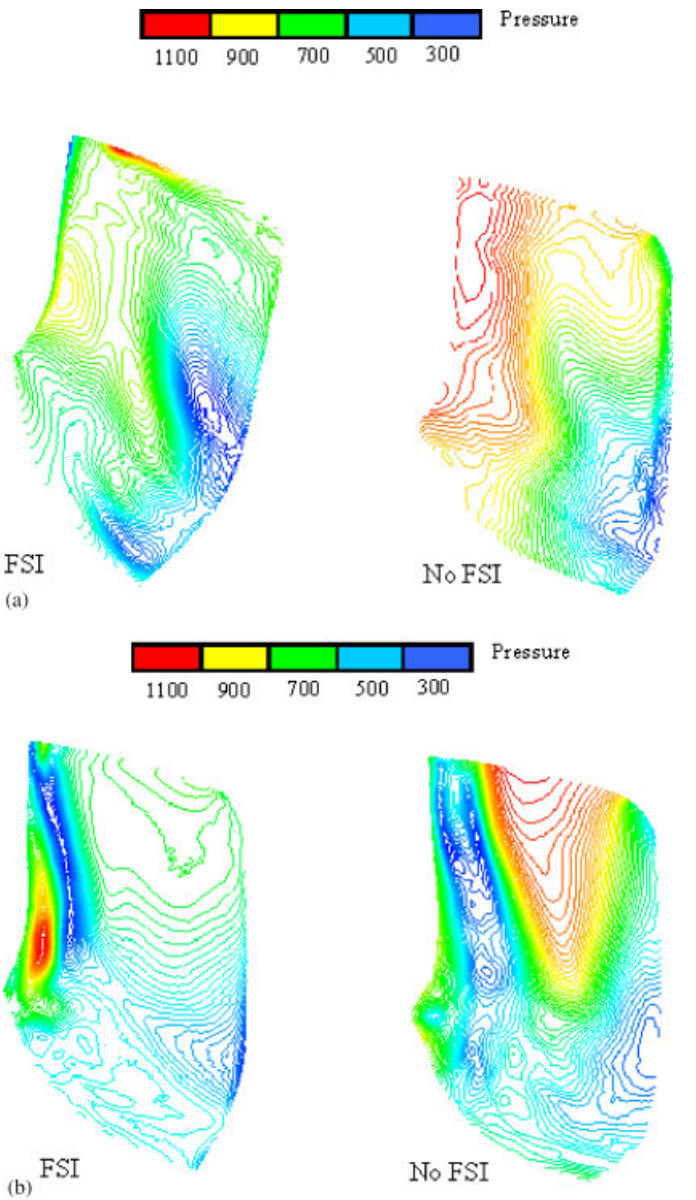

Figure 8. Static pressure distributions based on the time-averaged root-mean-square (RMS) (unit: Pa): (a) static pressure contours on the pressure surface and (b) static pressure contours on the suction surface.

in Figure 3, in which the numbers in brackets (•) represent the measured points on the suction side. The comparisons of the computations for the two cases and the measured pressures at these points are shown in Figure 10. We can see a better agreement between our computations with FSI and the experimental data as a whole, while failing to predict the pressure of point 2 near the

DOI: 10.1002/fld

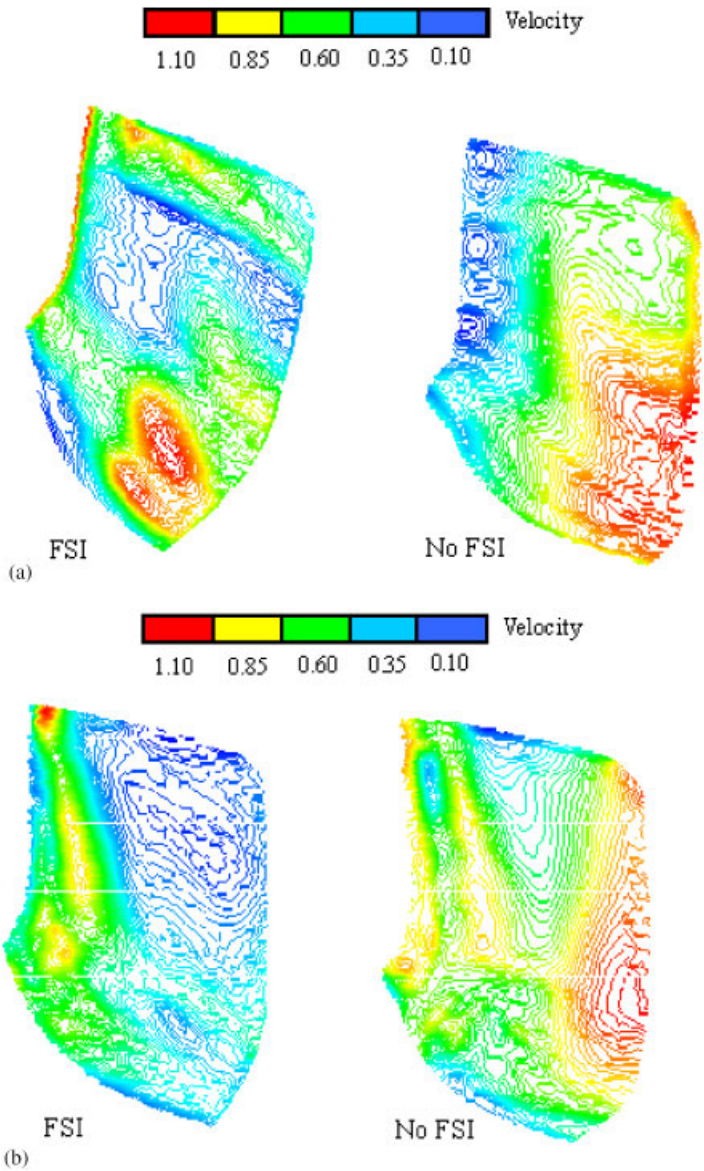

Figure 9. Velocity distributions based on the time-averaged root-mean-square (RMS) (unit: m/s): (a) velocity contours near the pressure surface and (b) velocity contours near the suction surface.

trailing edge of the Sm line on the pressure side, which is the maximum deformation zone, as seen in Figure 5. This is possibly caused by the computational method, as more modes are needed when constructing the reduced-order model in flexible, easily deformed regions. Overall, the results in this paper show that the simulations in which FSI is considered are closer to the measure, and that

DOI: 10.1002/fld

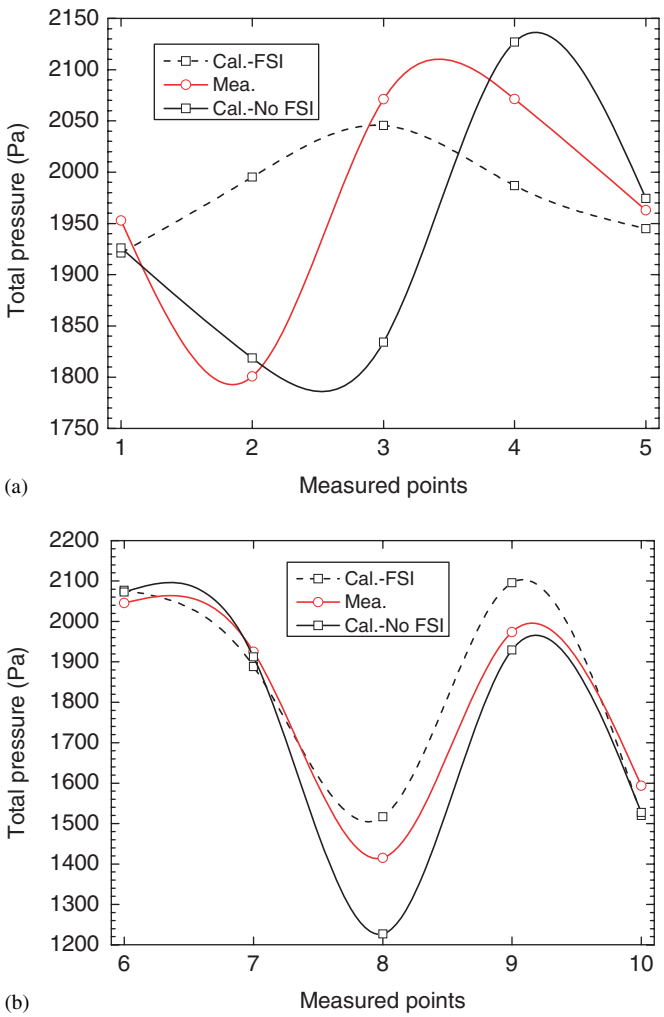

Figure 10. Comparisons of the computational and measured pressures on the sides of the blade: (a) pressure side and (b) suction side.

the results of LES in which FSI is considered for a high Reynolds number turbulence flow in a 3D complex geometrical passage are more credible.

The evolutions of the total pressure at four measured points are shown in Figure 11. From the comparisons between the calculated and the measured values, it can be seen that the predicted pressure fluctuation without FSI is far higher than the measured value on the suction side (points 8 and 10) and that it is lower than the measured value on the pressure side (points 3 and 4). In sum, a better agreement between our computations with FSI and with experimental data than that for computations without FSI is discovered, which confirms that computational results that consider FSI will be more accurate and also indicates that our coupled simulation strategy is credible.

DOI: 10.1002/fld

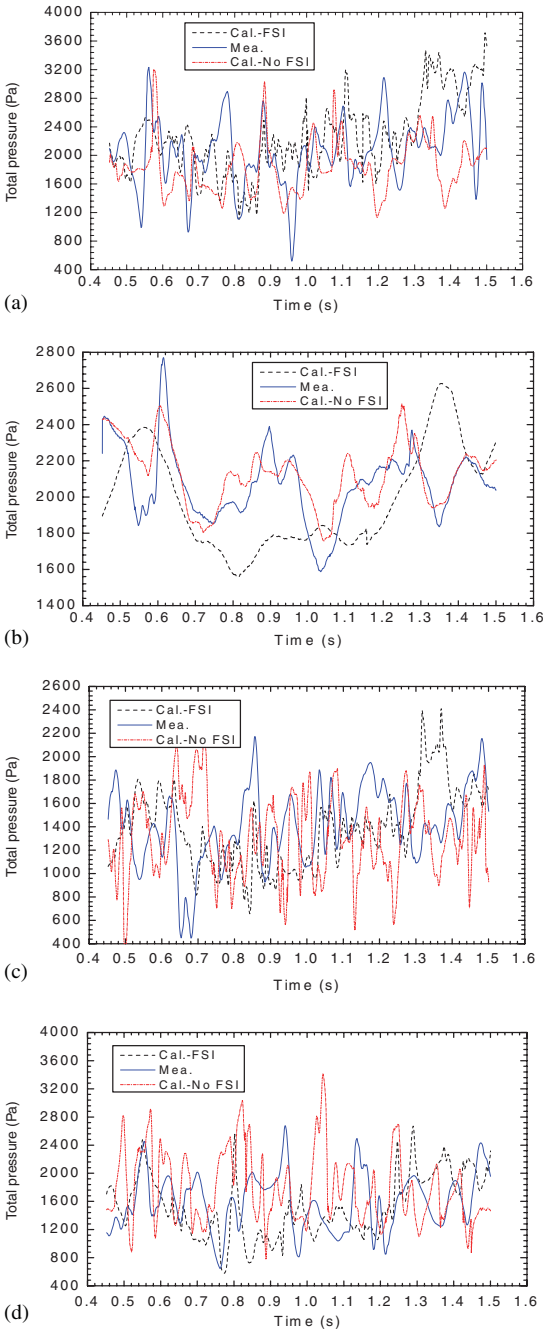

Figure 11. Comparison of the evolution of the computational and measured pressures on the sides of the blade: (a) point 3; (b) point 4; (c) point 8; and (d) point 10.

DOI: 10.1002/fld

5. CONCLUSIONS

We have proposed a very efficient coupling strategy that allows the strong coupling of partitioned solvers. This approach shows a very good convergence behavior with the construction of a reduced-order model for a fluid and structure solver that is based on only few stress and displacement modes. This model is used to compute the 3D incompressible turbulent flow in a complex geometry for a Francis hydroturbine in which the FSI is considered. Comparing the velocity and pressure fields, as well as the turbulence quantities of the runner inter-blade channel between the cases in which the FSI is considered and in which it is not considered, one can conclude that there is a large influence on the numerical results when considering the dynamic FSI. At the same time, a better agreement between our computations in which FSI is considered and the experimental data is obtained than in the case in which FSI is not considered, and therefore it is concluded that the coupling methodology and computational strategies we have presented in this paper are robust and suitable for the current 3D turbulent analysis or FSI-coupled analysis for both distributor and runner blades of Francis turbines. It is also possible to more accurately predict turbulent flow when FSI is considered in more engineering practice.

ACKNOWLEDGEMENTS

The authors thank the National Natural Science Foundation of China (NSFC) [Grant no. 50579025] for the financial support for this research.

REFERENCES

1. Vad J, Lajos T, Schilling R (eds). *Modelling Fluid Flow*: *The State of the Art*. Springer: Berlin, 2004; 269–434.
2. Friedrich R, Geurts BJ, Metais O. *Direct and Large-Eddy Simulation*. Kluwer Academic Press: Dordrecht, The Netherlands, 2004; 619–650.
3. Wu XH, Durbin PA. Evidence of longitudinal vortices evolved from distorted wakes in a turbine passage. *Journal of Fluid Mechanics* 2001; **446**:199–228.
4. Kalitzin G, Wu XH, Durbin PA. DNS of fully turbulent flow in a LPT passage. *International Journal of Heat and Fluid Flow* 2003; **24**:636–644.
5. Rodi W. DNS and LES of some engineering flows. *Fluid Dynamics Research* 2006; **38**:145–173.
6. Zhang LX, Wang WQ. LES of turbulent flow in 3D skew blade passage of a reacting hydro turbine. *Modern Physics Letters B* 2005; **19**(28/29):1487–1490.
7. Nilsson H, Davidson L. Validations of CFD against detailed velocity and pressure measurements in water turbine runner flow. *International Journal for Numerical Methods in Fluids* 2003; **41**:863–879.
8. Liu XB, Zeng YZ, Cao SY. Numerical predication of vortex flow in hydraulic turbine draft tube for LES. *Journal of Hydrodynamics*, *Series B* 2005; **17**:448–454.
9. Lai XD. Analysis and estimation of hydraulic stability of Francis hydro turbine. *Journal of Hydrodynamics*, *Series B* 2004; **16**:194–200.
10. Bathe KJ, Zhang H, Wang WH. Finite element analysis of incompressible and compressible fluid flows with free surfaces and structural interactions. *Computers and Structures* 1995; **56**:193–213.
11. Sarrate J, Huerta A, Donea J. Arbitrary Lagrangian–Eulerian formulation for fluid–rigid body interaction. *Computer Methods in Applied Mechanics and Engineering* 2001; **190**:3171–3188.
12. Rugonyi S, Bathe KJ. On finite element analysis of fluid flows fully coupled with structural interactions. *Computer Modeling in Engineering and Sciences* 2001; **2**:195–212.
13. Heil M. An efficient solver for the fully coupled solution of large-displacement fluid–structure interaction problems. *Computer Methods in Applied Mechanics and Engineering* 2004; **193**:1–23.
14. Cervera M, Codina R, Galindo M. On the computational efficiency and implementation of block-iterative algorithms for nonlinear coupled problems. *Engineering Computations* 1996; **13**:4–30.

DOI: 10.1002/fld

15. Piperno S. Explicit/implicit fluid–structure staggered procedures with a structural predictor and fluid subcycling for 2D inviscid aeroelastic simulations. *International Journal for Numerical Methods in Fluids* 1997; **25**:1207–1226.
16. Farhat C, Lesoinne M. Two efficient staggered algorithms for the serial and parallel solution of three-dimensional nonlinear transient aeroelastic problems. *Computer Methods in Applied Mechanics and Engineering* 2000; **182**:499–515.
17. Matthies HG, Steindorf J. Partitioned strong coupling algorithms for fluid–structure interaction. *Computers and Structures* 2003; **81**:805–812.
18. Guruswany GP, Byun C. Fluid–structure interaction using Navier–Stokes flow equations coupled with shell finite element structure. *AIAA 3087*, 1993.
19. Garica JA, Guruswany GP. Aeroelastic analysis of transonic wings using Navier–Stokes equations and a nonlinear beam finite element model. *AIAA 1215*, 1999.
20. Ramji K, Wei S. Fluid–structure interaction for aeroelastic applications. *Progress in Aerospace Sciences* 2004; **40**:535–558.
21. Zhang LX, Guo YK, Wang WQ. Large eddy simulation of turbulent flow in a true 3D Francis hydro turbine passage with dynamical fluid–structure interaction. *International Journal for Numerical Methods in Fluids* 2007; **54**:517–541.
22. Matthies HG, Niekamp R, Steindorf J. Algorithms for strong coupling procedures. *Computer Methods in Applied Mechanics and Engineering* 2006; **195**:2028–2049.
23. Liu F, Sadeghi M, Yang S, Tsai H. Parallel computation of wing flutter with a coupled Navier–Stokes/CSD method. *AIAA 1347*, 2003.
24. Liu F, Cai J, Zhu Y, Wong ASF, Tsai HM. Calculation of wing flutter by a coupled CFD-CSD method. *AIAA 0907*, 2000.
25. Vierendeels J. Implicit coupling of partitioned fluid–structure interaction solvers using a reduced-order model. In *Fluid–Structure Interaction*: *Modeling*, *Simulation*, *Optimization*, Bungartz HJ, Schafer M (eds). Springer: New York, 2006.
26. Smagorinsky J. General circulation experiments with the primitive equations: the basic experiment. *Monthly Weather Review* 1963; **91**:99–164.
27. Mochid A, Murakami S, Rodi W, Sakamoto S. Large eddy simulation of vortex shedding flow past 2D square cylinder. *Journal of Wind Engineering* 1993; **55**:79–80.
28. Suksangp A, Djilali N, Moinat P. Large-eddy simulation of separated flow over a bluerectangular plate. *International Journal of Heat and Fluid Flow* 2000; **21**:655–663.
29. Kogaki T, Koyayashi T. Large-eddy simulation of flow around a rectangular cylinder. *Fluid Dynamics Research* 1997; **20**:11–24.
30. Carstens V, Kemme R, Schmitt S. Coupled simulation of flow–structure interaction in turbomachinery. *Aerospace Science and Technology* 2003; **7**:298–306.
31. Sergent E. Vers une Méthodologie de Couplage entre la Simulation des Grandes Echelles et les Modèles Statistiques. *Ph.D. Thesis*, L'Ecole Centrale de Lyon, 2002.

DOI: 10.1002/fld